Nodal vacancy bound states and resonances in three-dimensional Weyl semimetals

J. P. Santos Pires,[1,2,*] S. M. João,[1,2] Aires Ferreira,[3] B. Amorim,[4] and J. M. Viana Parente Lopes[1,2,†]

[1] *Departamento de Física e Astronomia, Faculdade de Ciências da Universidade do Porto, Rua do Campo Alegre, s/n, 4169-007 Porto, Portugal*

[2] *Centro de Física das Universidades do Minho e do Porto (CF-UM-UP) and Laboratory of Physics for Materials and Emergent Technologies LaPMET, University of Porto, 4169-007 Porto, Portugal*

[3] *Department of Physics and York Centre for Quantum Technologies, University of York, YO10 5DD, York, United Kingdom*

[4] *Centro de Física das Universidades do Minho e do Porto (CF-UM-UP) and Laboratory of Physics for Materials and Emergent Technologies LaPMET, Universidade do Minho, 4710-057 Braga, Portugal*

The electronic structure of a cubic $\mathcal{T}$-symmetric Weyl semimetal is analyzed in the presence of atomic-sized vacancy defects. Isolated vacancies are shown to generate nodal bound states with r^{-2} asymptotic tails, even when immersed in a weakly disordered environment. These states show up as a significantly enhanced nodal density of states which, as the concentration of defects is increased, reshapes into a nodal peak that is broadened by inter-vacancy hybridization into a comb of satellite resonances at finite energies. Our results establish point defects as a crucial source of elastic scattering that leads to nontrivial modifications in the electronic structure of Weyl semimetals.

I. INTRODUCTION

With the advent of three-dimensional (3D) topological insulators [1, 2], the search for topological semimetals emerging at the transition between gapped phases of matter has flourished. Rather than being a fine-tuned situation, it was envisaged by Murakami [3] that, without inversion symmetry, topological phase transitions can proceed through an intermediate stage, in which a pair of two-fold degenerate band-crossing points moves around the first Brillouin zone until it finally merges together and gives rise to a new gapped phase. Such a stable gapless state was dubbed a Weyl semimetal (WSM) [4, 5] because low-energy excitations around these band-crossings are described by a decoupled pair of (3+1)–dimensional Weyl equations of opposite chirality [6]. Later on, such a topological gapless phase was also shown to be possible in centrossymetric crystals, so long as time-reversal symmetry is broken [7–10] (magnetic WSM). Crucially, in all cases, the band-crossings form pairs of point-like sources (or sinks) of Berry flux in momentum space, analogous to the well-known "diabolical points" described by Berry [11] in a generic two-level quantum system. Therefore, isolated Weyl nodes are topologically protected degeneracies in the electronic band structure that are robust to parametric changes of the Hamiltonian.

The topological character of WSMs yields important physical consequences, from the existence of surface Fermi arcs [7, 12–15] that connect Weyl nodes in the surface-projected first Brillouin zone (fBZ), to the remarkable condensed matter realization of QED's chiral anomaly [16, 17]. The latter drives distinctive unconventional transport effects, such as a negative longitudinal magnetoresistance [18, 19], a giant in-plane Hall effect [20, 21] and the chiral magnetic effect [22]. Nonetheless, perhaps the most remarkable property of a WSM is its resilience to the effects of unavoidable perturbations, such as disorder or crystal defects. From a theoretical standpoint, the study of disorder effects in both spectral [23–28] and transport properties [29–33] of WSMs have been the subject of intense research. A big focus was placed on the effects of random potentials that can yield non-Anderson quantum criticality at a finite disorder strength [29, 34, 35]. As the system is driven through this critical point, the semi-metallic character of the nodal single-electron states gets destroyed long before they become exponentially localized at the Anderson transition [24].

In contrast to conventional Anderson transitions [36, 37], the disorder-averaged nodal density of states (nDoS) in disordered WSMs is deemed an appropriate order parameter by field-theoretical calculations [30, 38–40], as well as the numerical observation of its sharp power-law growth above some critical disorder strength [24, 25, 41]. However, recent studies of nonperturbative instantonic effects have revealed that rare disorder configurations lift the nDoS and round-out its critical behavior [28, 42, 43], thus challenging the conventional scenario. A physical picture was then put forward by Nandkishore *et al* [42], who associated the nDoS lift to smooth rare-regions of a random potential landscape that can sporadically bound eigenstates at the nodal energy, giving way to an exponentially small but *nonzero* nDoS. Despite being a controversial proposal [25–27, 44–46], the *avoided* quantum criticality due to rare events was eventually confirmed in subsequent numerical studies [25–27] and it is now believed to be the most general scenario [28].

In spite of these numerous theoretical studies regarding the effects of random potential disorder, very little is known about the role played by point defects and other common disorder sources. Currently, time-reversal

* up201201453@fc.up.pt
† jlopes@fc.up.pt

symmetric Weyl fermions can be realized as low-energy quasiparticles in a myriad of materials, most notably within the TaAs cubic family (also including NbAs, TaP and NbP) [47], which can be grown as single crystals using chemical vapor transport techniques [48]. In the growth process, lattice defects are likely to form [49, 50] and, as demonstrated in previous experimental studies based on transmission electron microscopy [51] and Raman scattering [52], even high-quality samples generally host a considerable density of defects, mostly vacancies and stacking faults. Adding to their natural occurrence, vacancy defects can also be artificially induced by means of particle irradiation [53, 54], a well-tested technique previously used to generate defects in graphene [55] and two-dimensional semiconductors [56, 57]. Since point defects can significantly change the electronic structure of materials, a study of their impact as a source of disorder in WSMs opens up interesting possibilities. Promising results were reported by Xing *et al.* [58], where atomic vacancies hosted by the (magnetic) WSM $Co_3Sn_2S_2$ were linked to the presence of exotic localized spin–orbit polaron states on its surface. In this paper, we push this line forward by theoretically analyzing the electronic properties of Weyl fermions in the presence of point defects. More specifically, we characterize the electronic wavefunctions and corresponding density of states (DoS) of a lattice $\mathcal{T}$-symmetric Weyl semimetal with finite concentrations of randomly distributed atomic-sized vacancies with one (*half-vacancy*) or two (*full-vacancy*) orbitals missing from the defect sites.

The remainder of this paper is organized as follows. In Sec. II, we introduce our working model and a *projected Green's function formalism* (pGF) that is used to calculate the vacancy-induced DoS deformation and show that algebraically decaying nodal bound states appear for isolated half- and full-vacancies. In Sec. III, the existence of nodal bound states is further verified by *Lanczos diagonalization* [59–61] (LD) of lattices containing an isolated vacancy. The robustness of these states to an additional weakly disordered environment is also discussed. In Sec. IV, we analyze the averaged DoS of a WSM with a finite concentration of vacancies, employing a combination of LD and *spectral methods* [62–64]. While confirming that localized eigenstates still appear and enhance the value of the DoS around the Weyl node, our results further show that inter-vacancy hybridization quickly broadens the nodal peak in the DoS, forming a comb of symmetrically-placed subsidiary sharp resonances for a moderate concentration of defects. Finally, Sec. V summarizes our key results and gives an outlook.

II. MODELING AN ISOLATED VACANCY IN A WEYL SEMIMETAL

A lattice vacancy is a common crystalline defect [65]. When a crystal is formed some sites are not properly occupied by the corresponding atoms, creating a proportion of vacant sites [66, 67] that act as a source of disorder. In the language of tight-binding Hamiltonians, a vacancy can be modeled by removing one or more Wannier orbitals from a randomly chosen lattice site. We start by determining the effects of introducing a single lattice *half-* or *full-vacancy* in a two-band model of a WSM. We employ a particle-hole symmetric model that lives in a simple cubic lattice ($\mathcal{L}$) and features a low-energy dispersion relation with eight isotropic Weyl nodes pinned to the time-reversal invariant momenta of the cubic fBZ (see Fig. 1). The lattice Hamiltonian [28] may be written as

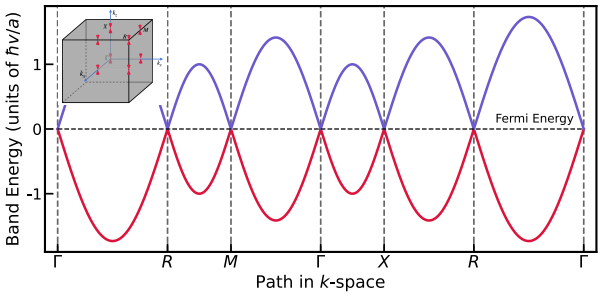

Figure 1. Band structure of the clean lattice WSM model along the $\boldsymbol{k}$-space path indicated in the inset. The locations of the eight non-equivalent Weyl cones are represented as well.

$$\mathcal{H}_0 = \frac{\hbar v}{2a} \sum_{\mathbf{R}\in\mathcal{L}} \sum_{i=x,y,z} \left[\Psi^\dagger_{\mathbf{R}} \cdot \sigma^i \cdot \Psi_{\mathbf{R}+a\hat{\mathbf{x}}_i} - \text{h.c.} \right] \tag{1}$$

where a is the lattice parameter, v is the Fermi velocity, $\hat{\mathbf{x}}_i = (\hat{x}, \hat{y}, \hat{z})$ are cartesian unit vectors, $\boldsymbol{\sigma}$ is the vector of 2×2 Pauli matrices and $\Psi^\dagger_{\mathbf{R}} = [c^\dagger_{\mathbf{R},1}, c^\dagger_{\mathbf{R},2}]$ is a local two-orbital fermionic creation operator. Equipped with this lattice description, the vacancy defects are implemented in two distinct ways. In our pGF calculations below, lattice vacancies are created by canceling all hoppings at the defect site, which leaves behind uncoupled zero energy Wannier states. In contrast, when the system is analyzed using spectral methods or LD [Secs. III and IV], the Hilbert space's dimension is effectively reduced by iterating with vectors orthogonal to the removed orbitals.

A. Clean Lattice Green Function and Nodal Point Symmetries

Before diving into the analysis of the electronic structure of WSMs with vacancy defects, we first establish some basic results. The Bloch Hamiltonian of the clean system admits the simple representation

$$\mathcal{H}_0(\mathbf{k}) = i\hbar v \boldsymbol{\sigma} \cdot \mathbf{sin}\, a\mathbf{k}, \tag{2}$$

with $\mathbf{sin}\, a\mathbf{k} \equiv (\sin ak_x, \sin ak_y, \sin ak_z)$, and which yields the dispersion relation represented in Fig. 1. The clean retarded lattice Green's function (LGF), defined formally as $G_0(E, \mathbf{R}_j - \mathbf{R}_i) = [E + i0^+ - \mathcal{H}_0]^{-1}_{\mathbf{R}_j,\mathbf{R}_i}$, can be written, in terms of dimensionless quantities, as

$$\boldsymbol{G}_0(\varepsilon, \boldsymbol{\Delta R}) = \int_{[-\pi,\pi]^3} \frac{d^{(3)}\boldsymbol{k}}{8\pi^3} \frac{\varepsilon + i\boldsymbol{\sigma}\cdot\mathbf{sin}\,\boldsymbol{k}}{\varepsilon^2 + |\mathbf{sin}\,\boldsymbol{k}|^2} e^{-i\mathbf{k}\cdot\boldsymbol{\Delta R}}, \tag{3}$$

where $\varepsilon = Ea/\hbar v + i\eta$ is the dimensionless energy (shifted by an imaginary amount η), $\boldsymbol{k}$ is the crystal momentum

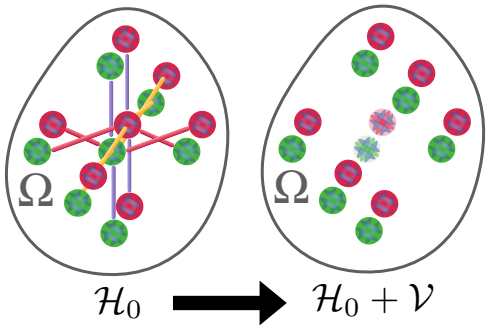

Figure 2. Scheme of the local perturbation defined in Eq. (9).

(in units of a^{-1}), $\boldsymbol{\Delta R}=(n_x,n_y,n_z)$, and $n_i\in\mathbb{Z}$ are indices that label particular sites. Equation (3) can be expressed in terms of four basic integrals over the domain $[-\pi,\pi]^3$, *i.e.*,

$$\boldsymbol{G}_0(\varepsilon,\boldsymbol{\Delta R})=\mathcal{I}^0_\varepsilon(\boldsymbol{\Delta R})-\sum_{j=x,y,z} i\sigma^j\,\mathcal{I}^j_\varepsilon(\boldsymbol{\Delta R})\,, \tag{4}$$

where the complex-valued integrals are

$$\mathcal{I}^0_\varepsilon(\boldsymbol{\Delta R})=\int_{[-\pi,\pi]^3} d^{(3)}\boldsymbol{k}\frac{\varepsilon\, e^{ik_xn_x}e^{ik_yn_y}e^{ik_zn_z}}{8\pi^3\left(\varepsilon^2+|\sin\boldsymbol{k}|^2\right)}\,, \tag{5a}$$

$$\mathcal{I}^x_\varepsilon(\boldsymbol{\Delta R})=\int_{[-\pi,\pi]^3} d^{(3)}\boldsymbol{k}\frac{\sin k_x e^{ik_xn_x}e^{ik_yn_y}e^{ik_zn_z}}{8\pi^3\left(\varepsilon^2+|\sin\boldsymbol{k}|^2\right)}, \tag{5b}$$

with $\mathcal{I}^{y,z}_\varepsilon(\boldsymbol{\Delta R})$ being obtained from $\mathcal{I}^x_\varepsilon(\boldsymbol{\Delta R})$ by a cyclic permutation of the set (n_x,n_y,n_z). These integrals can be numerically evaluated with high precision (see Appendix A) and display useful symmetry properties. First, the parity of the integrand dictates that $\boldsymbol{G}_0(E,\boldsymbol{\Delta R})=0$ whenever the set (n_x,n_y,n_z) contains more than one odd integer. This small-scale property of the LGF can be traced back to the existence of eight non-equivalent valleys which are specific to this lattice model. Additionally, there are non-spatial symmetries which can be deduced from Eqs. (5a)-(5b), most notably

$$\mathcal{I}^0_\varepsilon(\boldsymbol{\Delta R})=\left[\mathcal{I}^0_{\varepsilon^*}(\boldsymbol{\Delta R})\right]^* \tag{6a}$$

$$\mathcal{I}^j_\varepsilon(\boldsymbol{\Delta R})=-\left[\mathcal{I}^j_{\varepsilon^*}(\boldsymbol{\Delta R})\right]^* \tag{6b}$$

and also

$$\mathrm{Re}\left[\mathcal{I}^0_{i0^+}(\boldsymbol{\Delta R})\right]=\lim_{\eta\to0^+}\int_{[-\pi,\pi]^3} d^{(3)}\boldsymbol{k}\frac{\eta\,\sin\left(\boldsymbol{k}\cdot\boldsymbol{\Delta R}\right)}{8\pi^3\left(\eta^2+|\sin\boldsymbol{k}|^2\right)}=0, \tag{7}$$

by employing the cubic symmetry of the fBZ. Together, these three properties imply that the LGF at $E=0$ can be represented in the simple form

$$\boldsymbol{G}_0(0,\boldsymbol{\Delta R})=\sum_{j=x,y,z}\sigma^j\,\mathrm{Im}\left[\mathcal{I}^j_{i0^+}(\boldsymbol{\Delta R})\right], \tag{8}$$

which is non-zero if and only if $\boldsymbol{\Delta R}=(n_x,n_y,n_z)$ features a single odd integer.

B. Projected Green's Function for a Lattice Vacancy

Within a lattice description, a vacancy can be modeled by removing hoppings connecting one (or several) orbitals within a unit cell to its neighbors. With no loss of generality, let us consider a vacancy at the origin, $\boldsymbol{R}=\boldsymbol{0}$. The Hamiltonian is then $\mathcal{H}=\mathcal{H}_0+\mathcal{V}$ with

$$\mathcal{V}=-\frac{\hbar v}{2a}\sum_{i=x,y,z}\left[\Psi^\dagger_{\boldsymbol{0}}\cdot\sigma^i\cdot\Psi_{\boldsymbol{0}+a\hat{\mathbf{x}}_i}-\Psi^\dagger_{\boldsymbol{0}}\cdot\sigma^i\cdot\Psi_{\boldsymbol{0}-a\hat{\mathbf{x}}_i}-\mathrm{h.c.}\right]. \tag{9}$$

This operator has the advantage of having a finite support, *i.e.*, it acts only on sites $\Omega=\{\boldsymbol{0},\pm a\hat{\mathbf{x}}_1,\pm a\hat{\mathbf{x}}_2,\pm a\hat{\mathbf{x}}_3\}$ that form the octahedron shown in Fig. 2. Such local perturbations to a lattice model can be conveniently studied by using the pGF method. Treating $\mathcal{V}$ as a perturbation, we obtain a set of Dyson's equations for the system's Green's function, $\boldsymbol{G}(\varepsilon)$, in the presence of the vacancy, *i.e.*,

$$\boldsymbol{G}(\varepsilon)=\boldsymbol{G}_0(\varepsilon)+\boldsymbol{G}(\varepsilon)\cdot\mathcal{V}\cdot\boldsymbol{G}_0(\varepsilon) \tag{10a}$$

$$\boldsymbol{G}(\varepsilon)=\boldsymbol{G}_0(\varepsilon)+\boldsymbol{G}_0(\varepsilon)\cdot\mathcal{V}\cdot\boldsymbol{G}(\varepsilon), \tag{10b}$$

where $\cdot$ denotes the matrix product defined in the full Hilbert space. To solve these equations, we proceed in two steps: *i)* By projecting them into Ω, we can solve for those entries of the full $\boldsymbol{G}(\varepsilon)$, *i.e.*,

$$\overline{\boldsymbol{G}}(\varepsilon)=\left[\mathcal{I}-\overline{\boldsymbol{G}_0}(\varepsilon)\cdot\mathcal{V}\right]^{-1}\cdot\overline{\boldsymbol{G}_0}(\varepsilon), \tag{11}$$

where $\overline{\boldsymbol{G}_0}(\varepsilon)$ is the clean lattice Green's function restricted to Ω, with $\mathcal{I}-\overline{\boldsymbol{G}_0}(\varepsilon)\cdot\mathcal{V}$ defined within the (finite-dimensional) Hilbert subspace of Ω, and *ii)* The continuation of $\boldsymbol{G}(\varepsilon)$ to the exterior of Ω is obtained via

$$\boldsymbol{G}(\varepsilon)=\boldsymbol{G}_0(\varepsilon)+\boldsymbol{G}_0(\varepsilon)\cdot\overline{\mathcal{T}_\varepsilon}\cdot\boldsymbol{G}_0(\varepsilon), \tag{12}$$

where

$$\begin{aligned}\overline{\mathcal{T}_\varepsilon}&=\mathcal{V}+\mathcal{V}\cdot\overline{\boldsymbol{G}}(\varepsilon)\cdot\mathcal{V}\\&=\mathcal{V}\cdot\left[\mathcal{I}-\overline{\boldsymbol{G}}_0(\varepsilon)\cdot\mathcal{V}\right]^{-1}\end{aligned} \tag{13}$$

is the projected T-matrix of the vacancy.

The pGF method provides access to the electronic structure of an isolated impurity or defect embedded in an otherwise perfect infinite crystal [45, 68]. In the present section, we are interested in *i)* the DoS change induced by a vacancy, and *ii)* the possibility that a WSM can host nodal bound states around the vacancy. The emergence of zero-energy modes due to disorder is not obvious given the absence of non-spatial symmetries in our model; note that $\mathcal{H}_0$ belongs to the orthogonal Wigner-Dyson class (class AI in the Altland-Zirnbauer ten-fold classification [28]). This is to be contrasted to the well-studied case of graphene (chiral orthogonal BDI class [69, 70]), which supports zero-energy states localized around point defects whose peculiar spectral and transport properties have been linked to the underlying chiral symmetry of that model [63, 71].

One of the most readily available observable from the pGF formalism is the change in the (extensive) DoS due

to the vacancy, $\delta\nu(\varepsilon)$. This can be evaluated by means of equation,

$$\begin{aligned}\delta\nu(\varepsilon) &= \frac{1}{\pi n_b}\mathrm{Im}(\mathrm{Tr}\left[\boldsymbol{G}_0(\varepsilon)-\boldsymbol{G}(\varepsilon)\right]) \\ &= -\frac{1}{\pi n_b}\mathrm{Im}\Big(\mathrm{Tr}\left[\mathcal{V}\cdot[\mathcal{I}-\boldsymbol{G}_0(\varepsilon)\cdot\mathcal{V}]^{-1}\cdot\left(\boldsymbol{G}_0(\varepsilon)\right)^2\right]\Big) \\ &= \frac{1}{\pi n_b}\mathrm{Im}\left(\mathrm{tr}\left[\overline{\mathcal{T}_\varepsilon}\cdot\frac{d}{d\varepsilon}\boldsymbol{G}_0(\varepsilon)\right]\right), \end{aligned} \tag{14}$$

where $\overline{\mathcal{T}_\varepsilon}$ is the projected T-matrix, $\mathrm{Tr}\left[\cdots\right]$ is the trace operation over all degrees of freedom, $\mathrm{tr}\left[\cdots\right]$ is a trace over the support of $\mathcal{V}$, Ω, and n_b is the number of orbitals per unit cell (n_b=2 in the WSM model). In the last step to obtain Eq. (14), we have used Eq. (13) as well as the identity $d\boldsymbol{G}_0(\varepsilon)/d\varepsilon = -\left(\boldsymbol{G}_0(\varepsilon)\right)^2$.

Next, we discuss briefly how to extract information on bound states within the pGF framework. We start by writing the Lippmann-Schwinger equation for a scattering state $|\Psi_\varepsilon\rangle$,

$$|\Psi_\varepsilon\rangle = \left|\Psi^0_\varepsilon\right\rangle + \boldsymbol{G}_0(\varepsilon)\cdot\mathcal{V}\,|\Psi_\varepsilon\rangle\,, \tag{15}$$

where $\left|\Psi^0_\varepsilon\right\rangle$ is an eigenstate of the unperturbed system, which is the parent extended state of $|\Psi_\varepsilon\rangle$. In contrast, a bound state can exist without any parent eigenstate of the clean Hamiltonian. Thus, an eigenstate bound by $\mathcal{V}$ at an energy ε_b must be a solution of

$$|\Psi_{\varepsilon_b}\rangle = \boldsymbol{G}_0(\varepsilon_b)\cdot\mathcal{V}\,|\Psi_{\varepsilon_b}\rangle\,. \tag{16}$$

Since the perturbation $\mathcal{V}$ has a finite support, one can once again consider the projected version of Eq. (15),

$$|\xi_\varepsilon\rangle = \overline{\boldsymbol{G}_0}(\varepsilon)\cdot\mathcal{V}\,|\xi_\varepsilon\rangle\,, \tag{17}$$

where $|\xi_{\varepsilon_b}\rangle$ is the restriction of $|\Psi_{\varepsilon_b}\rangle$ to the support Ω. Thereby, any bound state must obey the condition,

$$\left[\mathcal{I}-\overline{\boldsymbol{G}_0}(\varepsilon_b)\cdot\mathcal{V}\right]\left|\xi^b_{\varepsilon_b}\right\rangle = 0, \tag{18}$$

which means that its projected wavefunction must belong to the kernel of the operator, $\mathcal{I}-\overline{\boldsymbol{G}_0}(\varepsilon_b)\cdot\mathcal{V}$. Outside the support of $\mathcal{V}$ the wavefunction may be reconstructed using

$$\Psi^b_\alpha(\mathbf{R}) = \left\langle\mathbf{R},\alpha\mid\Psi^b_{\varepsilon_b}\right\rangle = \langle\mathbf{R},\alpha|\boldsymbol{G}_0(\varepsilon_b)\cdot\mathcal{V}\left|\xi^b_{\varepsilon_b}\right\rangle, \tag{19}$$

which may or may not amount to a normalizable state, depending on the asymptotic behavior of the clean LGF. In this context, since we are looking for zero-energy modes (ε_b=0), any state obeying Eq. (18) is guaranteed to be square-normalizable in 3D space with an algebraic tail $\propto r^{-2}$. The latter is the long-distance behavior of $\boldsymbol{G}_0(0,\boldsymbol{\Delta R})$, as obtained in the continuum limit.

1. *Full-Vacancies in a Weyl Semimetal*

We now apply the general formalism described above to the case of a *full-vacancy* where both orbitals are removed from a particular lattice cell. To perform the calculation, it comes in handy to order the sites of Ω as $\{\mathbf{0}, a\hat{x}, a\hat{y}, a\hat{z}, -a\hat{x}, -a\hat{y}, -a\hat{z}\}$. With this ordering, one obtains $\mathcal{V}$ as the matrix

$$\mathcal{V} = \frac{\hbar v}{2a}\begin{bmatrix}\mathbb{O}_{2\times2} & -\boldsymbol{\sigma} & \boldsymbol{\sigma}\\ \boldsymbol{\sigma}^T & \mathbb{O}_{6\times6} & \mathbb{O}_{6\times6}\\ -\boldsymbol{\sigma}^T & \mathbb{O}_{6\times6} & \mathbb{O}_{6\times6}\end{bmatrix}, \tag{20}$$

within the projected subspace, while, by exploiting the symmetries of $\mathbf{G}_0$ [Eqs. 6a and 6b], we are able to further express the pGF as

$$\overline{\boldsymbol{G}_0}(0) = \frac{a}{i\hbar v}\begin{bmatrix}\mathbb{O}_{2\times2} & g_0\boldsymbol{\sigma}-g_0\boldsymbol{\sigma}\\ -g_0\boldsymbol{\sigma}^T & \mathbb{O}_{6\times6} & \mathbb{O}_{6\times6}\\ g_0\boldsymbol{\sigma}^T & \mathbb{O}_{6\times6} & \mathbb{O}_{6\times6}\end{bmatrix}, \tag{21}$$

where $g_0 = \mathcal{I}^x_{i0^+}(1,0,0)$. These simple matrices can then be used to build the operator $\mathcal{I}-\overline{\boldsymbol{G}_0}(0)\cdot\mathcal{V}$, whose determinant takes the remarkably simple form,

$$\det\left(\mathcal{I}-\overline{\boldsymbol{G}_0}(0)\cdot\mathcal{V}\right) = (i-3g_0)^4\,. \tag{22}$$

Equation (22) has a clear physical interpretation: a *four-fold degenerate* root appears for $g_0 = i/3$, corresponding to an extra pair of non-trivial bound states extending into the lattice. For consistency, $\det\left(\mathcal{I}-\overline{\boldsymbol{G}_0}(0)\cdot\mathcal{V}\right)$ would have to display a *two-fold degenerate* root, corresponding to the subspace of both orbitals to be removed from the lattice. Surprisingly, the degeneracy appears doubled here, which indicates that two nodal bound states must exist as a mathematical property of a full-vacancy in our lattice model. In addition, a full diagonalization of $\mathcal{I}-\overline{\boldsymbol{G}_0}(0)\cdot\mathcal{V}$ yields the following projected wavefunctions for these states:

$$\begin{aligned}\left|\xi^b_1\right\rangle = \frac{1}{\sqrt{6}}\big[&|\hat{\mathbf{x}},1\rangle - i\,|\hat{\mathbf{y}},1\rangle - |\hat{\mathbf{z}},2\rangle \\ &- |-\hat{\mathbf{x}},1\rangle + i\,|-\hat{\mathbf{y}},1\rangle + |-\hat{\mathbf{z}},2\rangle\big]\,,\end{aligned} \tag{23a}$$

$$\begin{aligned}\left|\xi^b_2\right\rangle = \frac{1}{\sqrt{6}}\big[&|\hat{\mathbf{x}},2\rangle + i\,|\hat{\mathbf{y}},2\rangle + |\hat{\mathbf{z}},1\rangle \\ &- |-\hat{\mathbf{x}},2\rangle - i\,|-\hat{\mathbf{y}},2\rangle - |-\hat{\mathbf{z}},1\rangle\big]\,,\end{aligned} \tag{23b}$$

where $|\mathbf{R},\alpha\rangle$ are the local Wannier states (here, α indexes the orbital). Upon a reconstruction, these states have the following real-space wavefunction outside Ω:

$$\Psi^b_1(\mathbf{R}) = \frac{it\sqrt{6}}{2}\begin{bmatrix}G^{12}_0(0,\mathbf{R})\\ G^{22}_0(0,\mathbf{R})\end{bmatrix} \tag{24a}$$

$$\Psi^b_2(\mathbf{R}) = \frac{it\sqrt{6}}{2}\begin{bmatrix}G^{11}_0(0,\mathbf{R})\\ G^{21}_0(0,\mathbf{R})\end{bmatrix}, \tag{24b}$$

where $G^{\alpha\beta}_0$ are spinor components of $\mathbf{G}_0$.

In a similar manner, we can determine the DoS change caused by a vacancy defect. To do this, we require the clean pGF at all energies, which has the following matrix structure,

$$\overline{\boldsymbol{G}_0}(\varepsilon) = \frac{a}{i\hbar v}\begin{bmatrix}f_\varepsilon\mathbb{I}_{2\times2} & g_\varepsilon\boldsymbol{\sigma} & -g_\varepsilon\boldsymbol{\sigma}\\ -g_\varepsilon\boldsymbol{\sigma}^T & f_\varepsilon\mathbb{I}_{6\times6} & h_\varepsilon\mathbb{I}_{6\times6}\\ g_\varepsilon\boldsymbol{\sigma}^T & h_\varepsilon\mathbb{I}_{6\times6} & f_\varepsilon\mathbb{I}_{6\times6}\end{bmatrix}, \tag{25}$$

as imposed by the aforementioned symmetries of our WSM model. In Eq. (25), $f_\varepsilon = \mathcal{I}^0_\varepsilon(0,0,0)$, $g_\varepsilon = \mathcal{I}^x_\varepsilon(1,0,0)$ and $h(\varepsilon) = \mathcal{I}^0_\varepsilon(2,0,0)$ are dimensionless functions of the energy variable. Having the pGF, we can now build the T-matrix of an isolated full-vacancy and employ Eq. (14) to obtain,

$$\delta\nu(\varepsilon) = \frac{3a}{\pi\hbar v}\mathrm{Im}\left[\frac{f_\varepsilon\,(h'_\varepsilon - 2f'_\varepsilon) + f'_\varepsilon h_\varepsilon - 4g'_\varepsilon\,(i+3g_\varepsilon)}{3f_\varepsilon^2 - 3f_\varepsilon h_\varepsilon + 2\,(i+3g_\varepsilon)^2}\right]. \quad (26)$$

The functions f_ε, g_ε and h_ε and their derivatives were calculated numerically (see Appendix A) and the resulting DoS is shown in Fig. 3. As expected, a single (full) vacancy causes a negative correction to the DoS across the entire band, which is consistent with an overall transfer of spectral weight to the emergent bound states around the vacant site. The integral of this curve is exactly -2, as the number of continuum states is not conserved, *i.e.*, two states (per orbital) appear as a vacancy bound-states and other two are removed from the Hilbert space.

2. *Half-Vacancies in Weyl Semimetals*

We now consider the effects of an isolated *half-vacancy* in which only one orbital is removed from each cell. If the orbital 1 is vacant, the perturbation reads

$$\mathcal{V}_1 = -\frac{\hbar v}{2a}\Big[(\psi^1_{\mathbf{0}})^\dagger\psi^2_{a\hat{x}} - i\,(\psi^1_{\mathbf{0}})^\dagger\psi^2_{a\hat{y}} + (\psi^1_{\mathbf{0}})^\dagger\psi^1_{a\hat{z}} - (\psi^1_{\mathbf{0}})^\dagger\psi^2_{-a\hat{x}} + i\,(\psi^1_{\mathbf{0}})^\dagger\psi^2_{-a\hat{y}} - (\psi^1_{\mathbf{0}})^\dagger\psi^1_{-a\hat{z}} - \mathrm{h.c.}\Big], \quad (27)$$

while in the opposite case, it reads

$$\mathcal{V}_2 = -\frac{\hbar v}{2a}\Big[(\psi^2_{\mathbf{0}})^\dagger\psi^1_{a\hat{x}} + i\,(\psi^2_{\mathbf{0}})^\dagger\psi^1_{a\hat{y}} - (\psi^2_{\mathbf{0}})^\dagger\psi^2_{a\hat{z}} - (\psi^2_{\mathbf{0}})^\dagger\psi^1_{-a\hat{x}} - i\,(\psi^2_{\mathbf{0}})^\dagger\psi^1_{-a\hat{y}} + (\psi^2_{\mathbf{0}})^\dagger\psi^2_{-a\hat{z}} - \mathrm{h.c.}\Big]. \quad (28)$$

In either situation, the presence of bound-states and DoS deformations can be investigated along the same lines of the *full-vacancy*, the only difference being the projected perturbation matrix. More specifically, we write

$$\mathcal{V}_{1/2} = \frac{\hbar v}{2a}\begin{bmatrix}\mathbb{O}_{2\times2} & -\boldsymbol{\Sigma}_{1/2} & \boldsymbol{\Sigma}_{1/2}\\ \boldsymbol{\Sigma}^T_{1/2} & \mathbb{O}_{6\times6} & \mathbb{O}_{6\times6}\\ -\boldsymbol{\Sigma}^T_{1/2} & \mathbb{O}_{6\times6} & \mathbb{O}_{6\times6}\end{bmatrix}, \quad (29)$$

where the (2×6)-dimensional $\boldsymbol{\Sigma}$–matrices are

$$\boldsymbol{\Sigma}_{\mathrm{u}} = \begin{bmatrix}0&1&0&-i&1&0\\0&0&0&0&0&0\end{bmatrix}, \quad (30a)$$

$$\boldsymbol{\Sigma}_{\mathrm{l}} = \begin{bmatrix}0&0&0&0&0&0\\1&0&i&0&0&-1\end{bmatrix}. \quad (30b)$$

The clean pGF is exactly the same as in Eq. (25), and therefore

$$\det\left(\mathcal{I} - \overline{\boldsymbol{G}_0}(0)\cdot\mathcal{V}_{1/2}\right) = -(i-3g_0)^2 \quad (31)$$

which has a double root for $g_0 = i/3$. The diagonalization of this operator confirms that its null-space is a two-dimensional subspace generated by the removed orbital, plus a non-trivial bound state that surrounds the vacant site. Similarly, the correction to the DoS is exactly the same as Eq. (26) but with an added factor of $1/2$. The similar behavior between *half-* and *full-vacancies* could have been anticipated by looking at a *full-vacancy* as a pair of *half-vacancies* placed within the same unit cell. In the pGF formalism, these correspond to local perturbations ($\mathcal{V}_1$ and $\mathcal{V}_2$) that act in disjoint Hilbert subspaces not connected by the clean lattice propagator. This prevents the two *half-vacancies* from hybridizing and their resulting effects in the spectrum will be simply cumulative. For this reason, we focus exclusively on *full-vacancies* in the remainder of this paper.

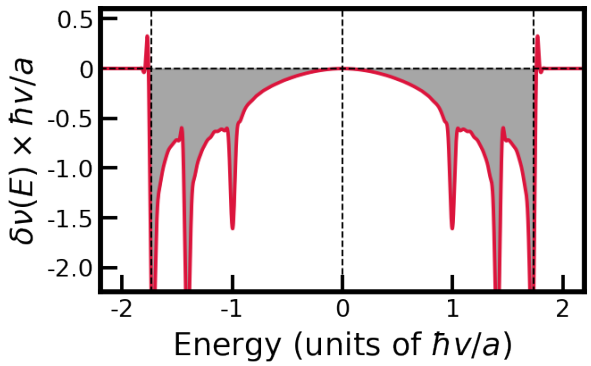

Figure 3. DoS correction due to a single (full) vacancy in an infinite lattice (calculated with numerical differentiation of the lattice GF). The unperturbed bandwidth of the model is marked by the outermost vertical dashed lines and, unlike the conventional case, integrating $\delta\nu(E)$ over the entire band yields -2 instead of zero.

III. MICROSCOPIC ROBUSTNESS OF THE VACANCY BOUND STATES

After establishing the existence of vacancy-induced nodal bound states, we move on to assess their robustness against additional disorder sources. For that, we model the additional disordered landscape as an uncorrelated scalar potential, $V_d(\boldsymbol{R})$. The Hamiltonian now reads

$$\mathcal{H}_d = \mathcal{H}_0 + \mathcal{V} + \sum_{\mathbf{R}\in\mathcal{L}} V_d(\boldsymbol{R})\Psi^\dagger_{\boldsymbol{R}}\cdot\Psi_{\boldsymbol{R}}. \quad (32)$$

To tackle this problem, we numerically diagonalize $\mathcal{H}_d$ around $E = 0$ using the `scipy` implementation of the implicitly restarted Lanczos method [59–61]. Since the method converges better to non-clustered eigenpairs in the borders of the spectrum, we apply it to $\mathcal{H}_d^2$ instead and restrict the analysis to low-lying eigenstates. Additionally, we consider cubic samples of side L, with a single (full) vacancy at the center of each sample, supplemented by fixed phase-twisted boundaries that open a finite-size gap ($\Delta_f \propto L^{-1}$) in the spectrum of extended states. The nodal bound states will lie inside this finite-size gap, as they are weakly affected by the boundary conditions.

In Fig. 4 a, we represent the radial distribution of the vacancy bound states for different simulation sizes, in the

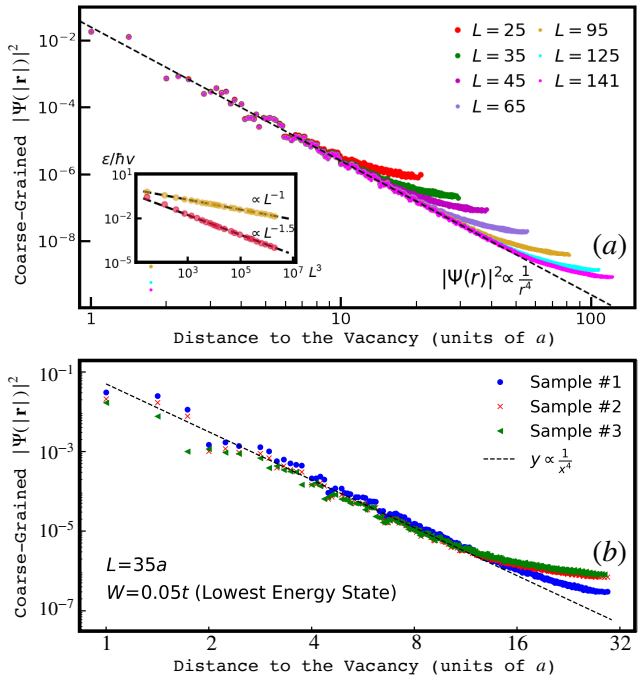

Figure 4. Probability density, $|\Psi(\mathbf{R})|^2 = |\Psi_1(\mathbf{R})|^2 + |\Psi_2(\mathbf{R})|^2$, of the eigenstate closest to zero averaged over spherical shells of width a centered on the vacancy. (a) Single central vacancy with no additional disorder. Inset: The eigenvalues obtained near $E=0$ for finite samples come in two flavors: those which scale to zero energy as L^{-1} (orange), akin to the predicted mean-level spacing scaling around a clean Weyl node, and eigenvalues which scale faster [as $\propto L^{-3/2}$] due to the more localized character of the corresponding eigenstate (magenta). (b) Vacancy within three random disordered environments.

absence of any additional disorder. The results confirm the predicted zero-energy states with tails decaying as r^{-2}. We note that the degeneracy of these states gets slightly lifted by the boundary conditions but the corresponding eigenvalues still tends to zero as $L^{-\frac{3}{2}}$, *i.e.,* faster than Δ_f. Furthermore, the vacancy defect perturbs slightly the extended states (now scattering states), which further expands the finite-size gap [72].

Next, we present an identical analysis with the vacancy's surroundings endowed with an uncorrelated random scalar potential uniformly drawn from $[-W/2, W/2]$. In principle, this alteration dresses the LGF of the clean model, thus *destroying most model-specific symmetries.* In Fig. 4 b, we present the radial wavefunctions of the two eigenstates closest to zero energy obtained from the diagonalization of three randomly generated disorder configurations. In all three cases, the states feature the same normalizable power-law tail found in the clean case, indicating that the vacancy bound states are indeed robust.

To further understand the effects of an uncorrelated disorder landscape, we diagonalized 10^4 systems with randomly generated disorder samples around a single central vacancy, focusing on determining the four eigenpairs whose energies are the closest to the node. In addition to the eigenenergies, we used the eigenfunctions to determine the inverse participation ratio (IPR),

$$\mathrm{IPR}_\Psi = \frac{\sum_{\mathbf{R}} \left(|\Psi^1_{\mathbf{R}}|^2 + |\Psi^2_{\mathbf{R}}|^2 \right)^2}{\sum_{\mathbf{R}} |\Psi^1_{\mathbf{R}}|^2 + |\Psi^2_{\mathbf{R}}|^2}, \tag{33}$$

a simple quantity that allows one to distinguish well localized, $\mathrm{IPR} \sim \mathcal{O}(1)$, from delocalized states, for which $\mathrm{IPR} \sim \mathcal{O}(L^{-3})$. In Fig. 5 a and 5 b, we show histograms of the eigenenergies for three system sizes and two disorder strengths, using twisted boundary conditions with a fixed twist angle of $\pi/3$ in all directions. These histograms borne out two well-separated clusters formed by: *(a)* the two eigenstates closest to zero energy which are broadened by disorder around $E=0$, but remain firmly inside the finite-size gap, and *(b)* the ones corresponding to the largest eigenvalues, being Bloch states that get perturbatively shifted towards the node and broadened by disorder [28]. As confirmed by the corresponding IPRs, the *(a)*-class states are strongly localized states which are still bound to the central vacancy, while the *(b)*-class are disorder-dressed extended Weyl states.

IV. QUANTUM-INTERFERENCE AND FINITE CONCENTRATION EFFECTS

The previous results established that a single (full) vacancy defect gives rise to a pair of zero-energy bound states with power-law-localized wavefunctions. We now discuss the effect of coherent multiple scattering events in realistic systems [51] which have a finite (nonzero) concentration of point defects. The main question we ask here is whether the essential IPR features of zero-energy states survive the unavoidable inter-vacancy hybridization effects.

Our starting approach to this problem is based upon the exact diagonalization of small systems. We consider WSM lattices with linear sizes up to $L = 35$ and a concentration (n) of randomly placed *full-vacancies.* By means of the twisted boundary conditions, we open a finite-size gap that separates nodal bound states from extended ones. The $2nL^3+4$ eigenpairs [73] closest to $E=0$ are then extracted using LD. In Fig. 5 c we represent a scatter plot of the energies and corresponding IPRs of every eigenpair determined for 2500 random arrangements of vacancies with concentrations ranging from 0.1% to 1% (per unit cell). The results clearly demonstrate that, in spite of the proximity between vacancies, the system still features a large number of high-IPR eigenstates which are flanked by a region of extended states. Such a physical interpretation is clear from Fig. 5 d, where a 3D bubble chart of $|\Psi(\mathbf{R})|^2$ is depicted for two eigenstates randomly chosen from each of the regions.

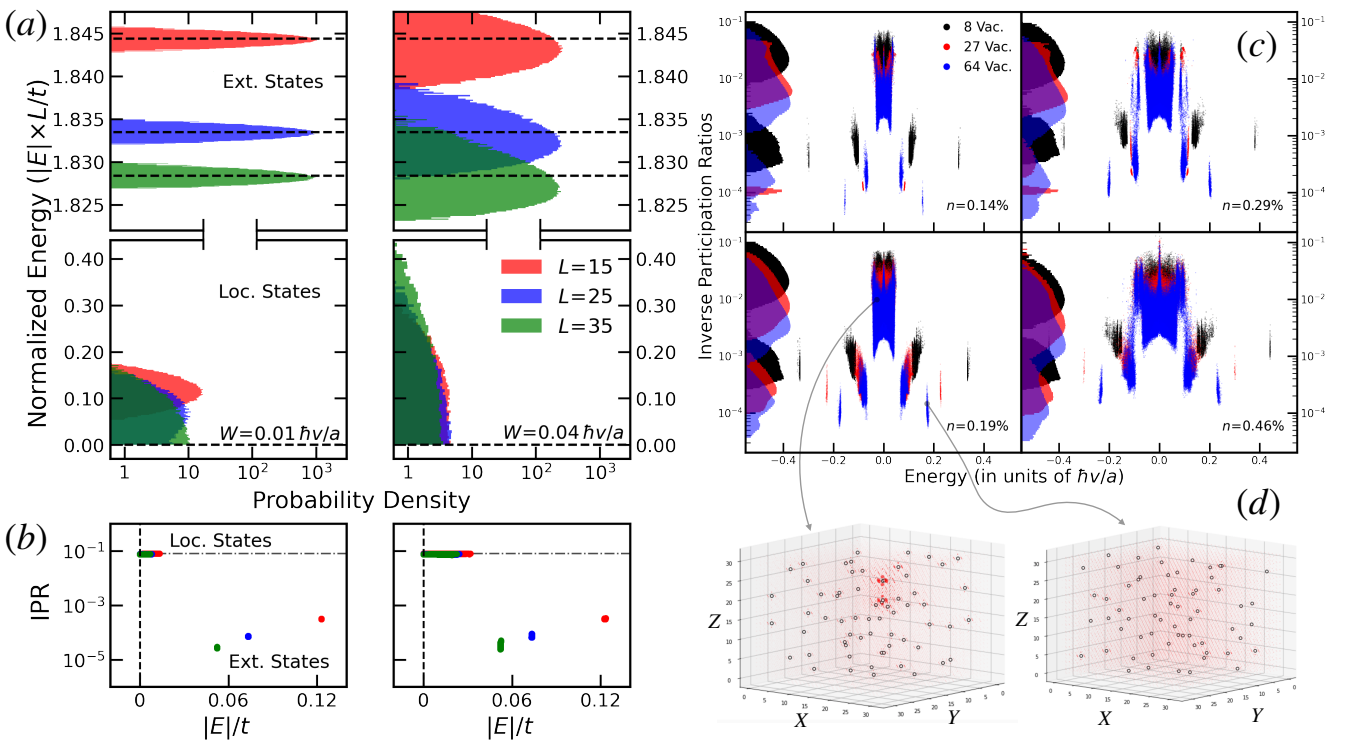

Figure 5. **(a)** Histograms of the four energies closest to the Weyl node for a vacancy surrounded by a random Anderson potential of strength $W = 0.01\hbar v/a$ (right) and $W = 0.04\hbar v/a$ (left), represented for systems with different linear sizes [$L = 15$ (red), $L = 25$ (blue) and $L = 35$ (red)]. Black dashed lines indicate the clean energy levels and, thus, the corresponding finite size gaps. **(b)** Scatter plot of the energies and IPRs of the calculated eigenpairs. The two eigenstates closest to zero energy are very localized in real-space, while the remaining pair is clearly delocalized. **(c)** Energy-IPR scatter plot for the eigenstates closest to the node obtained for 25000 samples of a WSM with four concentrations of randomly placed full-vacancies. Histograms of the IPRs are presented for each total number of vacancies along the vertical axis. Different colors label different vacancy numbers (here, the simulated cell size adjusted to guarantee that n is constant in all 4 cases presented). **(d)** Bubble chart representation of the (squared) wavefunctions for two eigenstates picked at random from the indicated regions: a heavily localized state around a few vacancies, (left) and an extended state (right).

A. Average Density of States

The LD study gives a qualitative picture of the structure of the eigenstates surrounding a Weyl node, but its utility can be severely limited by loss of spectral resolution, the finite number of eigenstates that are accessible and, lastly, the attainable system sizes. Therefore, we now complement the LD analysis with full-spectral simulations of the DoS of large systems by means of the *kernel polynomial method* (KPM) [62]. As a first step, we present results on the ensemble-averaged DoS for a large system with a linear size $L = 512$. This observable gives us information on how the spectrum is modified by inter-vacancy hybridization effects, yielding a numerically exact picture of the vacancy-induced resonances [27, 45] around the node. The KPM calculations are carried out with domain decomposition and a stochastic trace evaluation techniques as implemented in KITE [64]. The calculation employs $M = 2^{16}$ Chebyshev moments (corresponding to a spectral resolution $\eta = 10^{-4}\hbar v/a$), a Jackson kernel, and a sufficiently large number of random vectors to yield highly converged results. Finally, the results are averaged over random twisted boundary conditions which eliminates the finite size mean-level spacing.

The average DoS obtained through the KPM is shown in Fig. 6. These high-resolution results disclose a prominent spectral enhancement in and around the node which indicates that, unlike what happens for ordinary on-site disorder [23–28, 42, 44–46], the DoS at $E = 0$ gets quickly lifted to a large value as n increases. This pronounced effect is consistent with the presence of robust nodal bound states, and validates the conclusions of Sec. IV. Moreover, as the central DoS peak grows in height with increasing n, a much wider symmetrical profile begins to emerge at its base. As shown in Appendix B, the integral of this DoS correction is proportional to n, which indicates that inter-vacancy hybridization is simply turning the bound states of isolated (full) vacancies into scattering resonances within the continuum. In Fig. 6 b, a closeup of this structure is shown, revealing a finer *comb-like* structure of subsidiary peaks (sharp scattering resonances) around the node for moderate defect concentrations ($n \lesssim 1\%$). These peaks are more visible in Fig. 6 c, where their displacement as a function of n is also shown. The modulated structure in the DoS reported in this work is a unique feature of 3D WSMs, which is absent

in the analogous two-dimensional problem [63, 69] (see inset to Fig. 6 a). The subsidiary peaks in the DoS are robust to an additional weakly disordered potential, as is discussed in Appendix B.

V. CONCLUSION AND OUTLOOK

A combination of exact diagonalization and large-scale spectral methods allow us to resolve the impact of point defects on the real-space electronic structure of 3D $\mathcal{T}$-symmetric Weyl semimetals. Our results for a lattice WSM model show that dilute concentrations of vacancies, a common crystal imperfection, have a strong impact on the electronic properties in stark contrast with uncorrelated on-site disorder models [23–28, 31, 34, 42, 44–46, 74] which have been found to produce a minute effect on the low-energy properties of Weyl systems. In fact, random vacancies were shown to efficiently lift the nodal DoS thereby destabilizing the semi-metallic phase even at very low concentrations. Moreover, we have also demonstrated that quantum-interference effects between vacancies can yield a peculiar modulated energy dependence of electronic observables which has no analogue in two-dimensional Dirac systems [29, 63, 70]. While the average DoS displays a comb of subsidiary resonance peaks at finite energies, we show in a companion paper [75] that the bulk dc-conductivity mirrors this behavior through a series of sudden dips as the Fermi level is varied. Therefore, upon tuning the carrier density in real samples [76] [or even the defect concentration using H/He [53] or light-ion irradiation [54]], we predict that bulk transport measurements will allow the observation of interesting signatures of native point defects. These are expected to assume chief importance in WSMs of the TaAs family, whose concentration of point defects in high-quality crystals grown by chemical vapor transport is experimentally known to be large [51]. At last, in Ref. [75] the authors present a thorough investigation of physical consequences from these novel effects of vacancy disorder in electronic structure of the Weyl nodes, with a particular focus on experimentally accessible signatures from standard transport and optical response measurements. The optical signatures have a particular practical importance, as they do not rely on an external control over the system's Fermi energy.

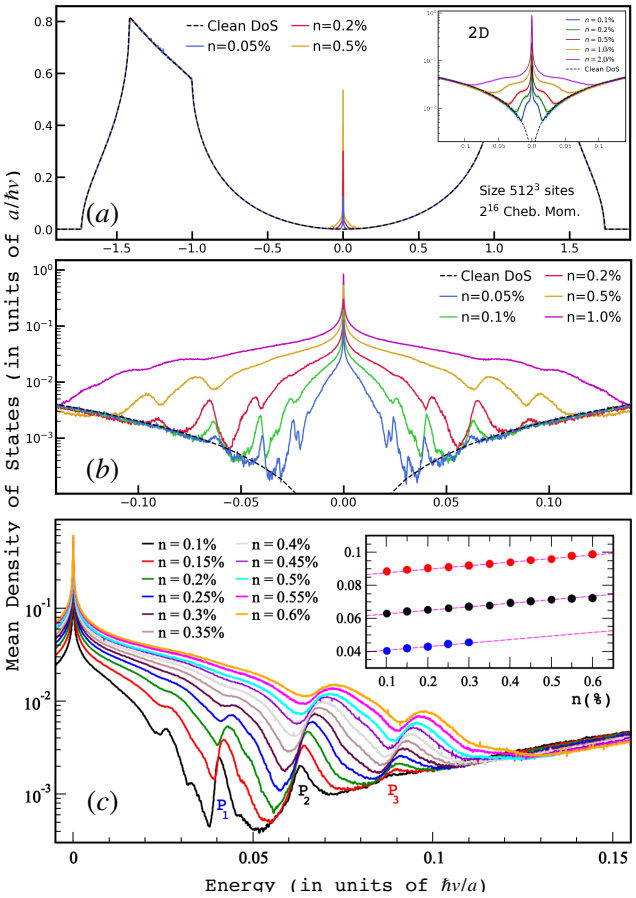

Figure 6. DoS of a WSM lattice of linear size $L = 512$ for selected defect concentrations. **(a)** Bird's-eye view of the DoS. The inset shows the two-dimensional case for comparison. **(b)** Close-up of average DoS around $\varepsilon = 0$. **(c)** Subsidiary peaks in the DoS at low vacancy concentration. Inset: Evolution of the the peak height (P_1, P_2 and P_3) with n.

ACKNOWLEDGMENTS

J.P.S.P., S.M.J, B.A. and J.M.V.P.L acknowledge support from the Portuguese Foundation for Science and Technology (FCT) within the Strategic Funding UIDB/04650/2020, and through projects No. POCI-01-0145-FEDER-028887 (J.P.S.P., S.M.J and J.M.V.P.L) and No. CEECIND/02936/2017 (B.A.). J.P.S.P. and S.M.J are funded by FCT grants No. PD/BD/142774/2018 and PD/BD/142798/2018, respectively. A.F. acknowledges support from the Royal Society (London) through a Royal Society University Research Fellowship. The large-scale calculations were undertaken on the HPC Viking Cluster of the University of York. We thank J. Dieplinger, J.M.B Lopes dos Santos and A. Altland for fruitful discussions. We also thank the anonymous referees for providing valuable feedback.

Appendix A: Lattice Green Function

Here, we outline the semi-analytical method employed to obtain the LGF with arbitrary spectral resolution. As indicated in the main text, Eqs. (3)-(4), the clean LGF is a 2×2 matrix that can be written as

$$\boldsymbol{G}_0(\varepsilon,\boldsymbol{\Delta R}) = \mathcal{I}^0_\varepsilon(\boldsymbol{\Delta R}) - \sum_{j=x,y,z} i\sigma^j \mathcal{I}^j_\varepsilon(\boldsymbol{\Delta R})\,, \tag{A1}$$

with $\mathcal{I}^{0,x,y,z}_\varepsilon(n_x, n_y, n_z)$ being four position- and energy-dependent integrals over the cubic fBZ. These integrals are given by

$$\mathcal{I}^0_\varepsilon(\boldsymbol{\Delta R}) = \int_{[-\pi,\pi]^3} d^{(3)}\mathbf{k} \frac{\varepsilon\, e^{ik_x n_x} e^{ik_y n_y} e^{ik_z n_z}}{8\pi^3 \left(\varepsilon^2 + |\sin \boldsymbol{k}|^2\right)} \tag{A2a}$$

$$\mathcal{I}^x_\varepsilon(\boldsymbol{\Delta R}) = \int_{[-\pi,\pi]^3} d^{(3)}\mathbf{k} \frac{\sin k_x e^{ik_x n_x} e^{ik_y n_y} e^{ik_z n_z}}{8\pi^3 \left(\varepsilon^2 + |\sin \boldsymbol{k}|^2\right)}, \tag{A2b}$$

For a single-vacancy calculation in the lattice WSM, the finite support of the perturbation dictates that only three of these integrals are required, namely:

$$\mathcal{I}^0_\varepsilon(0,0,0) = \int_{[-\pi,\pi]^3} d^{(3)}\mathbf{k} \frac{\varepsilon}{8\pi^3 \left(\varepsilon^2 + |\sin \boldsymbol{k}|^2\right)} \tag{A3a}$$

$$\mathcal{I}^x_\varepsilon(1,0,0) = \int_{[-\pi,\pi]^3} d^{(3)}\mathbf{k} \frac{\sin k_x e^{ik_x}}{8\pi^3 \left(\varepsilon^2 + |\sin \boldsymbol{k}|^2\right)} \tag{A3b}$$

$$\mathcal{I}^0_\varepsilon(2,0,0) = \int_{[-\pi,\pi]^3} d^{(3)}\mathbf{k} \frac{\varepsilon e^{2ik_x}}{8\pi^3 \left(\varepsilon^2 + |\sin \boldsymbol{k}|^2\right)}, \tag{A3c}$$

which define three complex-valued functions f_ε, g_ε and h_ε, respectively. In all previous integrals ε is to be taken as a complex number with a positive infinitesimal imaginary part (guaranteeing that the LGFs are retarded). In all three cases, analytical progress can be made by first considering the one-dimensional integral,

$$I_1(z) = \int_{-\pi}^{\pi} du \frac{1}{2\pi \left(z + \sin^2 u\right)} \tag{A4}$$

where $z \in \mathbb{C}$. This integral can be solved by standard contour integration in the complex variable $w = \exp(iu)$, yielding

$$I_1(z) = \frac{1}{\sqrt{z}\sqrt{z-1}}. \tag{A5}$$

Therefore,

$$I_1^{\pm}(x) = \lim_{\eta \to 0^{\pm}} [I_1(x + i\eta)] = \begin{cases} \frac{\mathrm{sgn}(x)}{\sqrt{x(x-1)}} & x \notin [0,1] \\ \mp \frac{i}{\sqrt{x(1-x)}} & x \in [0,1] \end{cases}. \tag{A6}$$

From Eq. (A6), it is easy to recognize that all three integrals in Eqs. (A3a)-(A3c) can be written as two-dimensional $\mathbf{k}$-integrals involving $I_1^{\pm}(x)$. Hence, they read

$$f_{E\pm i0^+} = \frac{E}{4\pi^2} \int_{[-\pi,\pi]^2} d^{(2)}\mathbf{k}\, I_1^{\pm}\left(E^2 + \sin^2 k_x + \sin^2 k_y\right) \tag{A7a}$$

$$g_{E\pm i0^+} = \frac{1}{4\pi^2} \int_{[-\pi,\pi]^2} d^{(2)}\mathbf{k} \sin k_x e^{ik_x}\, I_1^{\pm}\left(E^2 + \sin^2 k_x + \sin^2 k_y\right) \tag{A7b}$$

$$h_{E\pm i0^+} = \frac{E}{4\pi^2} \int_{[0,\pi]^2} d^{(2)}\mathbf{k} e^{2ik_x}\, I_1^{\pm}\left(E^2 + \sin^2 k_x + \sin^2 k_y\right), \tag{A7c}$$

where now E is the (real-valued) energy parameter and the $\pm$ denotes the sign of the energy. These two-dimensional integrals can be numerically evaluated for an arbitrarily fine mesh of E. As η was formally taken to zero, the spectral resolution is only limited by the spacing of this mesh. Moreover, using the symmetries — $f_{-E\pm i0^+} = -f^*_{E\pm i0^+}$, $g_{-E\pm i0^+} = g^*_{E\pm i0^+}$, $h_{-E\pm i0^+} = -h^*_{E\pm i0^+}$ — it is enough to evaluate the said integrals for $E > 0$. The results are shown in Fig. 7.

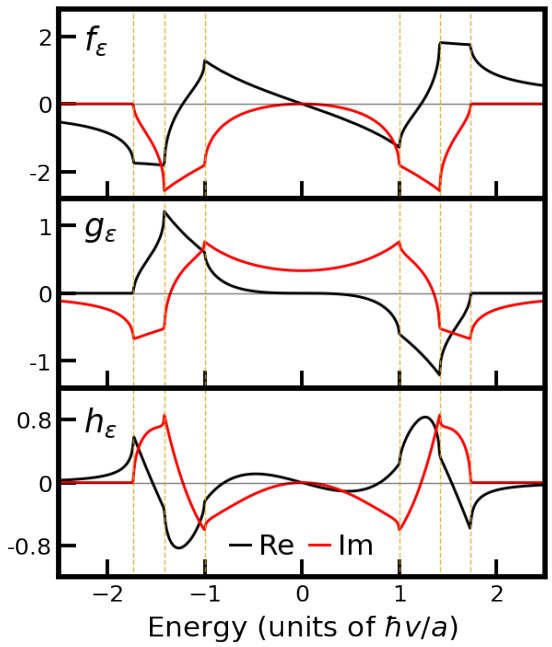

Figure 7. Numerical integrals that define the complex-valued functions f_ε, g_ε and h_ε. The node is placed at $\varepsilon = 0$. Van Hove singularities (derivative discontinuities) are marked as vertical dimmed lines. All the curves were obtained in an regular energy mesh of spacing $10^{-5}\hbar v/a$.

Appendix B: Additional Numerical Results

Here, we complement the KPM results shown in Sec. IV A for the mean DoS in the presence of a finite concentration of vacancies. These results serve as a support for some of the claims made in the main text.

First, we analyze the region of enhanced mean DoS around the nodal energy ($E = 0$). For a very low vacancy concentration, the sole feature is a sharp peak at the node, which amounts to a cumulative contribution of all single-vacancy bound states to the intensive DoS. As the concentration increases, one starts to see more structure, in the form of a broadened base of this peak (as highlighted in the main panel of Fig. 8 a). We attribute this to a progressive hybridization of states bound to nearby vacancies that lifts the degeneracies away from the node, thus turning these states into long-living resonances. To corroborate this idea, we analyze the dependence of the integrated change in the DoS within this central region. Broadly speaking, this quantity represents the number of states introduced near the node by the vacancies, per unit volume. In the inset to Fig. 8 a, we show that the integrated DoS change induced by the vacancies scales exactly as $n/(100-n)$. This is consistent with the picture

in which each missing Wannier state introduces exactly one eigenstate in the node and one eigenstate around the node.

Another point concerns with the robustness of the features of DoS to microscopic details of the underlying lattice model. As we have done for a single (full) vacancy, here also we probe this robustness by introducing an additional Anderson potential (of strength W). The KPM results for the mean DoS are shown in Fig. 8 b. Clearly, the main features of the DoS, *i.e.*, the central enhancement and the subsidiary peaks, remain untouched for suitably small W. This supports the claim that our results will hold for a wide range of WSM systems.

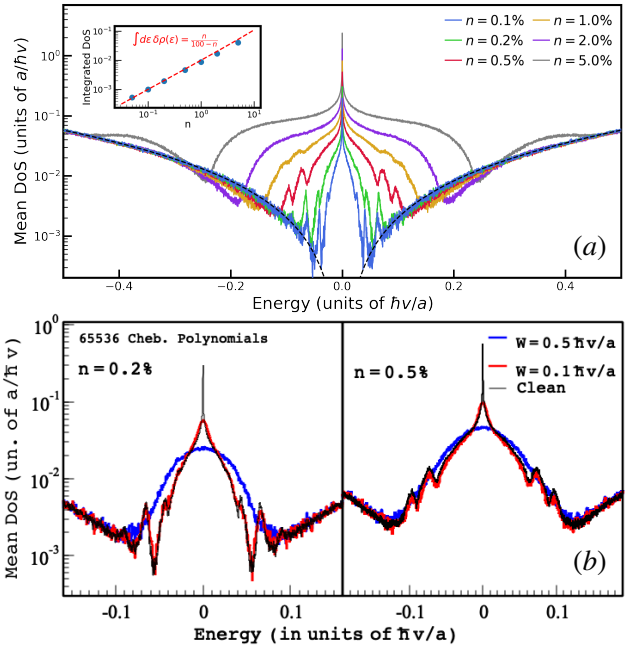

Figure 8. **(a)** Full integral of the correction do the mean DoS as a function of the vacancy concentration. Inset: Integral of $\delta\nu(\varepsilon) = \nu(\varepsilon) - \nu_0(\varepsilon)$ within the region represented plotted in the main panel. **(b)** Mean DoS calculated for two concentrations of vacancies and an additional potential disorder.

[1] L. Fu and C. L. Kane, Phys. Rev. B **76**, 045302 (2007).
[2] M. Z. Hasan and C. L. Kane, Rev. Mod. Phys. **82**, 3045 (2010).
[3] S. Murakami, New J. Phys. **9**, 356 (2007).
[4] G. B. Halász and L. Balents, Phys. Rev. B **85**, 035103 (2012).
[5] N. P. Armitage, E. J. Mele, and A. Vishwanath, Rev. Mod. Phys. **90**, 015001 (2018).
[6] H. Weyl, Proc. Natl. Acad. Sci. U.S.A. **15**, 323 (1929).
[7] X. Wan, A. M. Turner, A. Vishwanath, and S. Y. Savrasov, Phys. Rev. B **83**, 205101 (2011).
[8] G. Xu, H. Weng, Z. Wang, X. Dai, and Z. Fang, Phys. Rev. Lett. **107**, 186806 (2011).
[9] A. A. Burkov and L. Balents, Phys. Rev. Lett. **107**, 127205 (2011).
[10] M. Koshino and I. F. Hizbullah, Phys. Rev. B **93**, 045201 (2016).
[11] M. V. Berry, Proc. R. Soc. Lond. A. Math. Phys. Sci. , 45 (1984).
[12] P. Hosur, Phys. Rev. B **86**, 195102 (2012).
[13] E. Witten, Riv. del Nuovo Cimento **39**, 313 (2016).
[14] F. D. M. Haldane, arXiv:1401.0529.
[15] K. Hashimoto, T. Kimura, and X. Wu, Prog. Theor. Exp. Phys. **2017**, 053I01 (2017).
[16] S. L. Adler, Phys. Rev. **177**, 2426 (1969).
[17] J. S. Bell and R. Jackiw, Il Nuovo Cimento A (1965-1970) **60**, 47 (1969).
[18] D. T. Son and B. Z. Spivak, Phys. Rev. B **88**, 104412 (2013).
[19] C.-L. Zhang, S.-Y. Xu, I. Belopolski, Z. Yuan, Z. Lin, B. Tong, G. Bian, N. Alidoust, C.-C. Lee, S.-M. Huang, T.-R. Chang, G. Chang, C.-H. Hsu, H.-T. Jeng, M. Neu-

pane, D. Sanchez, H. Zheng, J. Wang, H. Lin, C. Zhang, H.-Z. Lu, S.-Q. Shen, T. Neupert, M. Zahid Hasan, and S. Jia, Nat. Comm. **7**, 10735 (2016).
[20] A. A. Burkov, Phys. Rev. B **96**, 041110(R) (2017).
[21] S. Nandy, G. Sharma, A. Taraphder, and S. Tewari, Phys. Rev. Lett. **119**, 176804 (2017).
[22] H. Nielsen and M. Ninomiya, Physics Letters B **130**, 389 (1983).
[23] S. Bera, J. D. Sau, and B. Roy, Phys. Rev. B **93**, 201302(R) (2016).
[24] J. H. Pixley, P. Goswami, and S. Das Sarma, Phys. Rev. Lett. **115**, 076601 (2015).
[25] J. H. Pixley, P. Goswami, and S. Das Sarma, Phys. Rev. B **93**, 085103 (2016).
[26] J. H. Wilson, D. A. Huse, S. Das Sarma, and J. H. Pixley, Phys. Rev. B **102**, 100201(R) (2020).
[27] J. P. Santos Pires, B. Amorim, A. Ferreira, İ. Adagideli, E. R. Mucciolo, and J. M. Viana Parente Lopes, Phys. Rev. Research **3**, 013183 (2021).
[28] J. Pixley and J. H. Wilson, Ann. Phys. , 168455 (2021).
[29] E. Fradkin, Phys. Rev. B **33**, 3263 (1986).
[30] B. Roy and S. Das Sarma, Phys. Rev. B **90**, 241112(R) (2014).
[31] S. V. Syzranov, L. Radzihovsky, and V. Gurarie, Phys. Rev. Lett. **114**, 166601 (2015).
[32] R.-J. Slager, V. Juričić, and B. Roy, Phys. Rev. B **96**, 201401(R) (2017).
[33] J. Shen, Q. Yao, Q. Zeng, H. Sun, X. Xi, G. Wu, W. Wang, B. Shen, Q. Liu, and E. Liu, Phys. Rev. Lett. **125**, 086602 (2020).
[34] S. V. Syzranov and L. Radzihovsky, Ann. Rev. Cond. Mat. Phys. **9**, 35 (2018).
[35] B. Roy, R.-J. Slager, and V. Juričić, Phys. Rev. X **8**, 031076 (2018).
[36] M. Janssen, Int. J. Mod. Phys. B **8**, 943 (1994).
[37] F. Evers and A. D. Mirlin, Rev. Mod. Phys. **80**, 1355 (2008).
[38] R. Shindou and S. Murakami, Phys. Rev. B **79**, 045321 (2009).
[39] P. Goswami and S. Chakravarty, Phys. Rev. Lett. **107**, 196803 (2011).
[40] S. V. Syzranov, V. Gurarie, and L. Radzihovsky, Phys. Rev. B **91**, 035133 (2015).
[41] K. Kobayashi, T. Ohtsuki, K.-I. Imura, and I. F. Herbut, Phys. Rev. Lett. **112**, 016402 (2014).
[42] R. Nandkishore, D. A. Huse, and S. L. Sondhi, Phys. Rev. B **89**, 245110 (2014).
[43] V. Gurarie, Phys. Rev. B **96**, 014205 (2017).
[44] M. Buchhold, S. Diehl, and A. Altland, Phys. Rev. Lett. **121**, 215301 (2018).
[45] M. Buchhold, S. Diehl, and A. Altland, Phys. Rev. B **98**, 205134 (2018).
[46] K. Ziegler and A. Sinner, Phys. Rev. Lett. **121**, 166401 (2018).
[47] B. Q. Lv, T. Qian, and H. Ding, Rev. Mod. Phys. **93**, 025002 (2021).
[48] N. J. Ghimire, Y. Luo, M. Neupane, D. J. Williams, E. D. Bauer, and F. Ronning, J. Phys.: Condens. Matt. **27**, 152201 (2015).
[49] J. Buckeridge, D. Jevdokimovs, C. R. A. Catlow, and A. A. Sokol, Phys. Rev. B **94**, 180101(R) (2016).
[50] Z. G. Yu and Y.-W. Zhang, Phys. Rev. B **94**, 195206 (2016).
[51] T. Besara, D. A. Rhodes, K.-W. Chen, S. Das, Q. R. Zhang, J. Sun, B. Zeng, Y. Xin, L. Balicas, R. E. Baumbach, E. Manousakis, D. J. Singh, and T. Siegrist, Phys. Rev. B **93**, 245152 (2016).
[52] H. W. Liu, P. Richard, L. X. Zhao, G.-F. Chen, and H. Ding, J. Phys.: Condens. Matt. **28**, 295401 (2016).
[53] Z.-J. Zhang, Y.-L. Fu, W. Cheng, and F.-S. Zhang, Computational Materials Science **160**, 9 (2019).
[54] Y.-L. Fu, H.-B. Sang, W. Cheng, and F.-S. Zhang, Mater. Today Commun. **24**, 100939 (2020).
[55] O. Lehtinen, J. Kotakoski, A. V. Krasheninnikov, A. Tolvanen, K. Nordlund, and J. Keinonen, Phys. Rev. B **81**, 153401 (2010).
[56] Z. Lin, B. R. Carvalho, E. Kahn, R. Lv, R. Rao, H. Terrones, M. A. Pimenta, and M. Terrones, 2D Mater. **3**, 022002 (2016).
[57] F. Bertoldo, S. Ali, S. Manti, and K. S. Thygesen, npj Computational Materials **8**, 56 (2022).
[58] Y. Xing, J. Shen, H. Chen, L. Huang, Y. Gao, Q. Zheng, Y.-Y. Zhang, G. Li, B. Hu, G. Qian, L. Cao, X. Zhang, P. Fan, R. Ma, Q. Wang, Q. Yin, H. Lei, W. Ji, S. Du, H. Yang, W. Wang, C. Shen, X. Lin, E. Liu, B. Shen, Z. Wang, and H.-J. Gao, Nat Commun **11**, 5613 (2020).
[59] C. Lanczos, J. Res. Natl. Inst. Stand. Technol. **45**, 255 (1950).
[60] C. Paige, Linear Algebra Appl. **34**, 235 (1980).
[61] R. Lehoucq and D. C. Sorensen, SIAM J. Matrix Anal. Appl **17**, 789 (1996).
[62] A. Weiße, G. Wellein, A. Alvermann, and H. Fehske, Rev. Mod. Phys. **78**, 275 (2006).
[63] A. Ferreira and E. R. Mucciolo, Phys. Rev. Lett. **115**, 106601 (2015).
[64] S. M. João, M. Anđelković, L. Covaci, T. G. Rappoport, J. M. Viana Parente Lopes, and A. Ferreira, R. Soc. open Sci. **7**, 191809 (2020).
[65] R. Siegel, Journal of Nuclear Materials **69-70**, 117 (1978).
[66] J. H. Crawford and L. M. Slifkin, *Point Defects in Solids* (Springer, Berlin, Germany, 1972).
[67] H.-E. Schaefer, K. Frenner, and R. Würschum, Phys. Rev. Lett. **82**, 948 (1999).
[68] G. D. Mahan, Int. J. Mod. Phys. B **9**, 1313 (1995).
[69] V. M. Pereira, F. Guinea, J. M. B. Lopes dos Santos, N. M. R. Peres, and A. H. Castro Neto, Phys. Rev. Lett. **96**, 036801 (2006).
[70] P. M. Ostrovsky, I. V. Protopopov, E. J. König, I. V. Gornyi, A. D. Mirlin, and M. A. Skvortsov, Phys. Rev. Lett. **113**, 186803 (2014).
[71] C.-K. Chiu, J. C. Y. Teo, A. P. Schnyder, and S. Ryu, Rev. Mod. Phys. **88**, 035005 (2016).
[72] This difference is too small to be seen in the inset of Fig. 4 and does not affect the asymptotic scaling of Δ_f with the system size.
[73] We expect each vacancy to generate a pair of bound states, making this number sufficiently large to capture most states within the finite-size gap.
[74] S. Syzranov, V. Gurarie, and L. Radzihovsky, Ann. Phys. **373**, 694 (2016).
[75] J. P. Santos Pires, S. M. João, A. Ferreira, B. Amorim, and J. M. Viana Parente Lopes, arXiv:cond-mat/2205.15123 (2022).
[76] S. Nishihaya, M. Uchida, Y. Nakazawa, M. Kriener, Y. Kozuka, Y. Taguchi, and M. Kawasaki, Sci. Adv. **4**, eaar5668 (2018).